
Convergence of finite element right-hand-side computation from finite difference data

Stefan Schoder

Institute of Fundamentals and Theory of Electrical Engineering
 Graz University of Technology
 8010 Graz, Austria
 stefan.schoder@tugraz.at

Abstract

This work presents two integration methods for field transfer in computational aeroacoustics and in coupled field problems, using the finite element method to solve the acoustic field. Firstly, a high-order Gaussian quadrature computes the finite element right-hand side. In contrast, the (flow) field provided by the finite difference mesh is mapped by higher-order B-Splines or a Lagrangian function. Secondly, the cut-cell or supermesh integration with geometric clipping. For each method, the accuracy, performance characteristics, and computational complexity are analyzed. As a reference, the trapezoidal integration rule was computed from the finite difference results. The high-order quadrature converges as the B-Spline interpolation order increases, and the finite difference results and mesh resolutions are consistent. The supermesh approach eliminates interpolation and approximation errors at the grid-to-mesh level and improves accuracy. This behaviour is universal for smooth or strongly oscillating field quantities, which will be shown in a comparative study between the Lighthill-like source term and the source term of the perturbed convective wave equation for subsonic flows.

1 Introduction

Hybrid finite difference-finite element methods for computational aeroacoustics [1] require accurate field transfer [2] between structured finite difference grids and unstructured finite element method meshes. The finite element right-hand side assembly for acoustic source terms requires the evaluation of

$$\mathbf{b}_i = \int_{\Omega} N_i(\mathbf{x}) f(\mathbf{x}) d\Omega, \quad (1)$$

where $N_i(\mathbf{x})$ are finite element shape functions and $f(\mathbf{x})$ is the source field defined on a structured finite difference grid. Note that this approach is not limited to finite differences but can also be applied when a structured or unstructured finite volume scheme provides the input field. In the following, the implementation details, accuracy, and performance of the presented schemes are presented. A comparative study evaluated the specific differences of different aeroacoustic source terms of acoustic equations, like the ones derived in [3, 4, 5, 6, 7, 8]. The visualizations in [4, 5, 6] show that the Lighthill-like source terms are more spatially varying and have sharper transitions as the source term exhibiting by the aeroacoustic wave equation based on Pierce operator or the extension of the perturbed convective wave equation to subsonic flows. The visual inspections suggest that interpolating smoother source terms may be less prone to errors arising from spatial discretisation.

2 Methods

2.1 High-Order Gaussian Quadrature with Higher-Order Accurate Field Interpolation

The finite element method right-hand side assembly uses Gaussian quadrature within each element

$$\mathbf{b}_i = \sum_{e=1}^{N_e} \int_{\Omega_e} N_i(\mathbf{x}) f_{\text{interp}}(\mathbf{x}) d\Omega \approx \sum_{e=1}^{N_e} \sum_{q=1}^Q w_q N_i(\boldsymbol{\xi}_q) f_{\text{interp}}(\mathbf{x}_q) |\mathbf{J}(\boldsymbol{\xi}_q)|, \quad (2)$$

where $Q = n_{\text{gauss}}^2$ is the number of quadrature points per element, \mathbf{J} is the Jacobian matrix, and f_{interp} is interpolated from the finite difference grid points to the Gauss quadrature points. It is important that for this type of right-hand side integration, both the interpolation order of the field function as well as the quadrature order must be sufficiently high to converge properly. Furthermore, mesh information is exchanged between the finite difference grid and the finite element mesh. The field interpolation is carried out by B-Splines supporting the orders $p \in \{1, 2, 3, 4, 5\}$ (as provided by `scipy.interpolate.RectBivariateSpline` in Python 3.10.13 `scipy` 1.11.4) or Lagrangian polynomials of the orders $p \in \{1, 3\}$.

For the B-spline interpolation in 2D, let $f_{ij} = f(x_i, y_j)$ be sampled on a uniform Cartesian grid with spacing h . The tensor-product B-spline interpolant of degree p is defined as

$$f_{\text{interp}}(x, y) = \sum_i \sum_j B_i^{(p)}(x) B_j^{(p)}(y) c_{ij}, \quad (3)$$

where $B_i^{(p)}$ denotes the cardinal B-spline basis function of degree p , and c_{ij} are the spline coefficients obtained from the data f_{ij} . The spline coefficients c_{ij} are determined by

$$f(x_i, y_j) = \sum_m \sum_n B_m^{(p)}(x_i) B_n^{(p)}(y_j) c_{mn}, \quad \forall i, j. \quad (4)$$

This yields a linear system of equations for the coefficients. For sufficiently smooth functions $f \in C^{p+1}$, B-spline interpolation of degree p achieves the error estimate

$$\|f - f_{\text{interp}}\| = \mathcal{O}(h^{p+1}). \quad (5)$$

The Lagrange interpolant of degree p is defined as

$$f_{\text{interp}}(x, y) = \sum_i \sum_j L_i^{(p)}(x) L_j^{(p)}(y) f_{ij}, \quad (6)$$

where $L_i^{(p)}(x)$ denotes the Lagrange basis polynomial of degree p , defined as

$$L_i^{(p)}(x) = \prod_{k=0}^p \frac{x - x_k}{x_i - x_k}. \quad (7)$$

The interpolation is performed in two steps: first, a 1D Lagrange interpolation is applied along the x -direction to compute intermediate values; second, the values are then interpolated along the y -direction to obtain the final interpolated value. For $p = 1$, this reduces to a bilinear interpolation. The bilinear interpolant uses two stencil points (respectively, the finite difference points) in each direction

$$f_{\text{interp}}(x, y) = (1 - d_x)(1 - d_y)f_{00} + d_x(1 - d_y)f_{10} + (1 - d_x)d_yf_{01} + d_xd_yf_{11}, \quad (8)$$

where $d_x = \frac{x - x_0}{x_1 - x_0}$ and $d_y = \frac{y - y_0}{y_1 - y_0}$. The Lagrange interpolation achieves the following error estimate for sufficiently smooth functions $f \in C^{p+1}$

$$|f - f_{\text{interp}}| = \mathcal{O}(h^{p+1}). \quad (9)$$

2.1.1 Algorithm

Algorithm 1 Right-hand side Assembly by High-Order Quadrature

Require: finite difference data $(x_{\text{fd}}, y_{\text{fd}}, f_{\text{fd}})$, finite element method mesh, interpolation order p , Gauss order n_g

Ensure: right-hand side vector $\mathbf{b} \in \mathbb{R}^{N_{\text{nodes}}}$

- 1: **Phase 1: Interpolator Construction**
- 2: Initialize interpolator with order p and finite difference grid points
- 3: **Phase 2: Quadrature Point Generation**
- 4: **for** each finite element $e = 1, \dots, N_e$ **do**
- 5: Generate $n_g \times n_g$ Gauss points in the local element reference coordinates ξ_q
- 6: Map to physical coordinates: $x_q = \mathbf{X}(\xi_q)$
- 7: **end for**
- 8: **Phase 3: Field Interpolation**
- 9: Vectorized interpolation: $\mathbf{f}_{\text{gauss}} = \text{interpolate}(f_{\text{fd}}, \{x_q\})$
- 10: **Phase 4: Assembly**
- 11: **for** each finite element e **do**
- 12: **for** each quadrature point q **do**
- 13: Evaluate shape functions: $\mathbf{N}_q = \mathbf{N}(\xi_q)$
- 14: Compute Jacobian: $J_q = \det(\mathbf{J}(\xi_q))$
- 15: Accumulate the right-hand side vector: $\mathbf{b}_{\text{local}} \leftarrow \mathbf{b}_{\text{local}} + w_q \mathbf{N}_q \mathbf{f}_{\text{gauss}}[q] J_q$
- 16: **end for**
- 17: Add (assemble) to the global right-hand side vector: $\mathbf{b} \leftarrow \mathbf{b}_{\text{local}}$
- 18: **end for**

2.1.2 Convergence Analysis

The convergence analysis assesses the accuracy of the finite-difference (fd) to finite-element method (fem) data transfer pipeline, which consists of three error components

$$\varepsilon_{\text{total}} = \varepsilon_{\text{interp}} + \varepsilon_{\text{quad}} + \varepsilon_{\text{fem}}. \quad (10)$$

For polynomial interpolation of order p , finite element basis function polynomial order r , and Gaussian quadrature of order $2q - 1$

$$\varepsilon_{\text{interp}} = \mathcal{O}(h_{\text{fd}}^{p+1}) \quad (11)$$

$$\varepsilon_{\text{quad}} = \mathcal{O}(h_{\text{fem}}^{2q}) \quad \text{if } 2q - 1 \geq p \quad (12)$$

$$\varepsilon_{\text{fem}} = \mathcal{O}(h_{\text{fem}}^{r+1}). \quad (13)$$

$\varepsilon_{\text{interp}}$ is the interpolation error from finite difference grid to finite element Gauss point locations, $\varepsilon_{\text{quad}}$ is the quadrature error in the integration, and ε_{fem} is the finite element method spatial discretization error. The interpolation order accuracy was confirmed by studying the analytical function $f(x, y) = \sin(k_x x) \sin(k_y y)$ with $k_x = k_y = 2.5\pi$. In doing so, the grid spacing $h_{\text{fd}} \in \{2.5 \cdot 10^{-2}, \dots, 1.5 \cdot 10^{-3}\}$ m was modified on a unit cube domain $[0; 1]^2$, and the evaluation (finite element 40x40 elements) mesh was fixed and 9-point Gauss quadrature per element used. The following relative error was computed $e_{\text{interp}}(h) = \|f_{\text{interp}} - f_{\text{analytic}}\|_{L^2(\Omega_{\text{fem}})} / \|f_{\text{analytic}}\|_{L^2(\Omega_{\text{fem}})}$. The B-spline interpolation was used to compute the evaluation in Fig. 1. In addition, a second study evaluated the convergence of the integral for the analytic function with $k_x = k_y = 4.5\pi$. The results presented in Fig. 2 show that the quadrature converges for a smooth function towards machine precision as the Gauss quadrature order is increased. For this test case, the analytic function was used to obtain the function values to be integrated directly, without interpolation. In a third testcase, the analytic function was first evaluated at a finite-difference location and then interpolated to the Gauss quadrature points using a Lagrangian bicubic $p = 3$ interpolation. The results are provided in Fig. 3. In the first execution, the calculation was rather slow because it was executed the first time and the respective function caches were created. In the error analysis, we can identify that for a Gauss quadrature order larger than four the interpolation error takes over and limits the overall precision of the algorithm. This is consistent with the following error estimate $E_{\text{quad}}(h) = \max(h_{\text{fd}}^{p+1}, h_{\text{fem}}^{2q})$, being in the limiting case $E_{\text{quad}}(h) = \max((1/1600)^4, (1/40)^8) = (1/40)^8$.

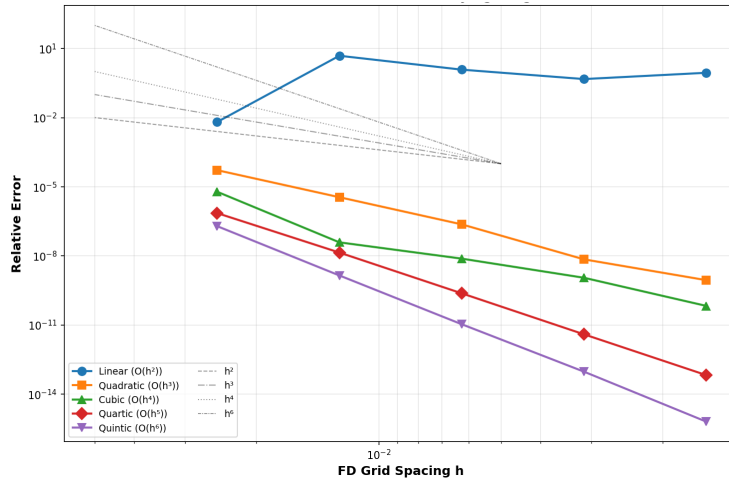


Figure 1: Interpolation error analysis as a function of finite difference grid spacing and interpolation order.

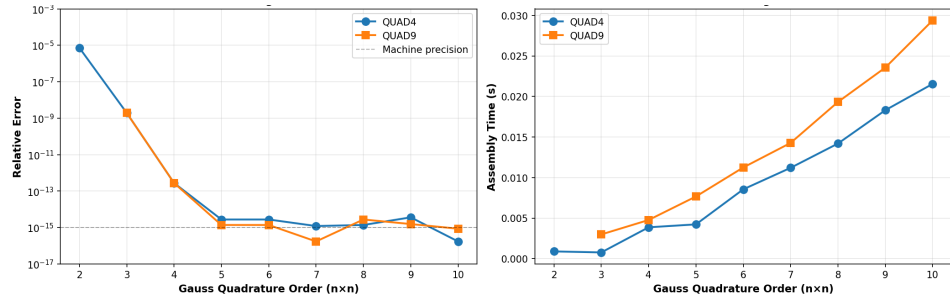


Figure 2: Interpolation error (left) and right-hand side assembly time of algorithm 1 (right) as a function of the Gauss quadrature order.

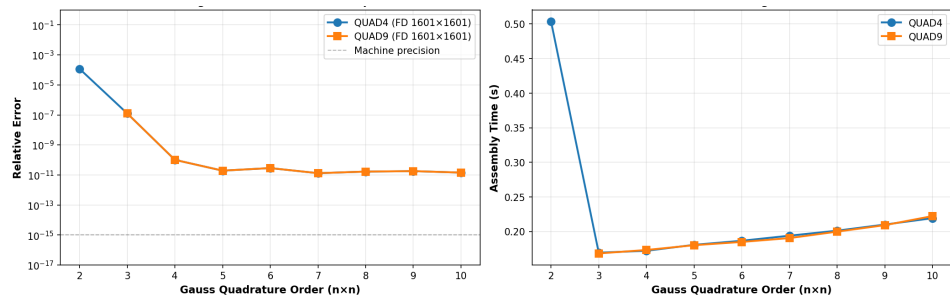


Figure 3: Interpolation error (left) and right-hand side assembly time of algorithm 1 (right) as a function of the Gauss quadrature order.

The practical implication of this study is that one cannot usually apply finite-difference grid refinement after the solution is already obtained. Still, if one wants to use this algorithm, high-order interpolation schemes are essential to consider to reduce the interpolation error that arises when increasing the quadrature order of the right-hand-side integration. A rule of thumb says both must be increased consistently to reduce the overall error. As a reference for the integral, the finite difference trapezoidal rule presented in the appendix can be used to quantify the error on the finite element mesh relative to the integral computed on the finite difference grid. This procedure is strongly recommended, since otherwise the algorithm cannot guarantee sufficient convergence in practice, where the field quantities may not be "sufficiently" smooth. Therefore, we are seeking to integrate aeroacoustic sources into a method that conservatively accounts for the right-hand-side source term (i.e., the complete energy from the flow field is transferred to the acoustic mesh without reduction) globally and locally [2]. The method presented in [2] only considers constant field values within one finite volume cell. For partial differential equation satisfaction while super resolving or interpolating the results, the hybrid Least Squares Support Vector Regression can be used [9].

2.2 Cut-Cell-based Supermesh Integration

In computational physics simulations, transferring fields across incompatible discretisations is challenging, especially when the integral of the field quantity (energy exchange) must be conserved. The cut-cell or supermesh (geometric overlay of two non-conforming meshes) integration method provides an integral-preserving field transfer by computing geometric intersections and performing quadrature on the intersected meshes, resulting in cut polygons. The problem statement is that, we have given a finite difference (or finite volume) grid $\Omega_{\text{fd}} = \{(x_i, y_j) : i = 0, \dots, n_x - 1, j = 0, \dots, n_y - 1\}$, with given finite difference field values $f_{\text{fd}}(x, y)$ defined on finite difference grid, and we have given a finite element mesh Ω_{fem} with N_e elements and N_n nodes. The goal is to compute the finite element right-hand side (load) vector

$$\mathbf{b}_i = \int_{\Omega_{\text{fem}}} N_i(\mathbf{x}) f_{\text{fd}}(\mathbf{x}) d\Omega. \quad (14)$$

The challenges in computing this integral are that the discretisation is often non-conforming, finite difference cells and finite elements have arbitrary overlap, the geometric complexity of computing polygon intersections is high, and the computational cost is therefore substantial compared to ordinary field interpolation methods.

2.2.1 Domain Decomposition

Let Ω_{fem}^e denote the e -th finite element and $\Omega_{\text{fd}}^{(i,j)}$ the finite difference cell at indices (i, j) , we can reformulate the integral to

$$\int_{\Omega_{\text{fem}}^e} N_k(\mathbf{x}) f_{\text{fd}}(\mathbf{x}) d\Omega = \sum_{(i,j)} \int_{\Omega_{\text{fem}}^e \cap \Omega_{\text{fd}}^{(i,j)}} N_k(\mathbf{x}) f_{\text{fd,interp}}(\mathbf{x}) d\Omega \quad (15)$$

where $\mathcal{P}_{e,(i,j)} = \Omega_{\text{fem}}^e \cap \Omega_{\text{fd}}^{(i,j)}$ defines an intersection polygon. The $f_{\text{fd,interp}}$ can be computed using the B-Spline (3), Lagrangian (6), or bilinear interpolation (8).

2.2.2 Integration

The integral is evaluated using Gauss quadrature at Gauss points distributed over the physical subcell of the supermesh. This does not mean that a parametric space exists for each subcell. The $f_{\text{fd,interp}}(\mathbf{x})$ can be evaluated on the real physical coordinates. The integration occurs in the reference coordinate system of the target element, not the subcell. Therefore, the mapping from the real physical coordinates (Gauss points) to the reference coordinates of the target element must be inverted.

The integration domain $\mathcal{P}_{e,(i,j)} \subset \Omega_{\text{fem}}^e$ is determined by geometric intersections in physical space, rather than fixed reference coordinates. Consequently, the quadrature points \mathbf{x}_q must be placed to capture the shape of the physical cut region $\mathcal{P}_{e,(i,j)}$. Evaluating the basis functions N_i at these physical points requires the inverse mapping $\xi_q = \mathbf{X}^{-1}(\mathbf{x}_q)$. For higher-order polynomial isoparametric elements or higher-order geometrically mapped finite elements, this inverse is not analytic and

Newton-Raphson might obtain inversion for every quadrature point:

$$\int_{\mathcal{P}_{e,(i,j)}} f_{\text{fd,interp}}(\mathbf{x}) N_i(\mathbf{x}) \, d\mathbf{x} = \sum_{q \in \text{cut}} f_{\text{fd,interp}}(\mathbf{x}_q) N_i(\mathbf{X}^{-1}(\mathbf{x}_q)) \det\left(\frac{\partial \mathbf{X}}{\partial \boldsymbol{\xi}}(\mathbf{X}^{-1}(\mathbf{x}_q))\right) w_q. \quad (16)$$

This introduces high computational cost and complexity compared to standard assembly, as the mapping $\mathbf{X}(\boldsymbol{\xi}_q)$ is designed to be evaluated explicitly only in the forward direction. To compute the quadrature on generalized intersection polygon $\mathcal{P}_{e,(i,j)}$, the polygon is tessellated into triangles $\{\mathcal{T}_1, \mathcal{T}_2, \dots, \mathcal{T}_{n_T}\}$. On each triangle \mathcal{T}_m , the 6-point Gaussian quadrature is used to integrate the right-hand side partly. The finite element method right-hand side vector component on element e for the local degree of freedom k is calculated as

$$b_k = \sum_{(i,j)} \sum_{m=1}^{n_T^{e,(i,j)}} |\mathcal{T}_m| \sum_{q=1}^6 w_q N_k(\mathbf{x}_q) f_{\text{fd,interp}}(\mathbf{x}_q), \quad (17)$$

where (i, j) are the finite difference cells intersecting element e , $n_T^{e,(i,j)}$ is the number of triangles in the intersection polygon $\mathcal{P}_{e,(i,j)}$, and $|\mathcal{T}_m|$ is the area of triangle m .

In standard finite element assembly, the right-hand side corresponding to an analytic forcing function $f(\mathbf{x})$ is assembled as

$$\int_{\Omega_e} f(\mathbf{x}) N_i(\mathbf{x}) \, d\mathbf{x} = \sum_q f(\mathbf{X}(\boldsymbol{\xi}_q)) N_i(\boldsymbol{\xi}_q) \det\left(\frac{\partial \mathbf{X}}{\partial \boldsymbol{\xi}}(\boldsymbol{\xi}_q)\right) w_q, \quad (18)$$

without requiring any inverse mapping or nonlinear iteration.

2.2.3 Physical space to target element reference mapping

A smooth, invertible transformation

$$\mathbf{x} = \mathbf{X}(\boldsymbol{\xi}), \quad \boldsymbol{\xi} \in \hat{\Omega}, \quad \mathbf{x} \in \Omega, \quad (19)$$

where $\hat{\Omega}$ denotes the reference element and \mathbf{X} is typically a polynomial or spline-based mapping of degree $p \geq 1$. This can be an expansion using the same basis functions as the finite element basis functions for isoparametric finite elements, or a different mapping function. Given a physical point $\mathbf{x}^* \in \Omega$ (the seeded Gauss points in real physical space), a pointwise evaluation of a finite element geometry mapping requires the corresponding reference coordinates $\boldsymbol{\xi}^*$ satisfying

$$\mathbf{X}(\boldsymbol{\xi}^*) = \mathbf{x}^*. \quad (20)$$

For linear mappings this inversion is analytic. However, for curvilinear or high-order geometry mapping \mathbf{X} is nonlinear and does not admit a closed-form inverse. Consequently, the reference coordinates $\boldsymbol{\xi}^*$ must be obtained by solving the nonlinear system

$$\mathbf{F}(\boldsymbol{\xi}) = \mathbf{X}(\boldsymbol{\xi}) - \mathbf{x}^* = \mathbf{0}. \quad (21)$$

This can be performed using a Newton-Raphson iteration, which is provided in the appendix.

2.2.4 Geometry Processing

Axis-Aligned Bounding Box (AABB) indexing is used to find finite difference cells that intersect a finite element efficiently. We use binary search on the structured grid to get a list of potential finite difference cell candidate indices (i, j) inside a target element bounding box $[x_{\min}, x_{\max}] \times [y_{\min}, y_{\max}]$. In general, the clipping of a finite element against an AABB is performed by the Sutherland-Hodgman polygon clipping algorithm [10] or the CGAL library.

2.2.5 Algorithm

The algorithm is separated into a setup phase and an execution phase, which is executed at every timestep of the simulation data.

Algorithm 2 Supermesh Integration Pipeline

Require: finite difference grid $(x_{\text{fd}}, y_{\text{fd}}, f_{\text{fd}})$, finite element method mesh, tolerance $\varepsilon = 10^{-10}$
Ensure: right-hand side vector \mathbf{b}

- 1: **Phase 1: AABB Spatial Indexing**
- 2: **for** each finite element e **do**
- 3: Compute element bounding box using $\text{AABB}_e = [\min x_e, \min y_e, \max x_e, \max y_e]$
- 4: Find candidate finite difference cells \mathcal{C}_e
- 5: **end for**
- 6: **Phase 2: Geometric Clipping**
- 7: **for** each element e and cell $c \in \mathcal{C}_e$ **do**
- 8: Create polygons $P_e = \text{Polygon}(e)$, $P_c = \text{Polygon}(c)$
- 9: $\Omega_{e,c} = \text{Intersection}(P_e, P_c)$
- 10: **end for**
- 11: **Phase 3: Sub-Tessellation**
- 12: **for** each intersection polygon $\Omega_{e,c}$ **do**
- 13: Triangulate $\{\mathcal{T}_k\} = \text{Tesselate}(\Omega_{e,c})$
- 14: **for** each triangle \mathcal{T}_k **do**
- 15: Map six-point Gauss quadrature rule to \mathcal{T}_k : $\{(\mathbf{x}_{kq}, w_{kq})\}_{q=1}^6$
- 16: **end for**
- 17: **end for**
- 18: **Phase 4: Field Evaluation**
- 19: **for** each Gauss point \mathbf{x}_{kq} **do**
- 20: **finite difference Evaluation:** $f_{\text{fd},\text{interp}}(\mathbf{x}_{kq}) = \text{Interp}(\mathbf{x}_{kq}, c)$
- 21: **finite element method Evaluation:**
- 22: Newton-Raphson: $\xi = \text{InverseMap}(\mathbf{x}_{kq}, e, \varepsilon)$
- 23: Shape functions: $N(\xi)$, Jacobian: $J(\xi)$
- 24: **Integration and Assembly:** $\mathbf{b} \leftarrow \mathbf{b} + w_{kq} N(\xi) f_{\text{fd}}(\mathbf{x}_{kq}) J(\xi)$
- 25: **end for**

3 Comparative study

The following CFD data from the case [6, 11, 12] is transformed from the finite difference grid $x/\delta_\omega \in [20, 150]$, $y/\delta_\omega \in [-15, 15]$ to the finite element mesh. $D\Phi_p/Dt$ and $\nabla \cdot \mathbf{F} = -\nabla \cdot [(\mathbf{u}_v \cdot \nabla) \mathbf{u}_v + (\mathbf{u}_0 \cdot \nabla) \mathbf{u}_v + (\mathbf{u}_v \cdot \nabla) \mathbf{u}_0]$ as an exemplary source term are considered (see Fig 4), for more detail we refer to [6]. In figure 5 and 6, the cut-cell supermesh geometric clipping, the bicubic B-spline interpolation with 3×3 Gauss quadrature, and the quintic B-spline interpolation with 4×4 Gauss quadrature are shown. All timings were measured after a warm-up run to ensure JIT compilation and cache-warming effects were excluded. The supermesh method converges to machine-precision for all mesh resolutions. In contrast, interpolation-based methods exhibit systematic errors that converge with mesh refinement, improved quadrature, and higher interpolation order. Furthermore, it can be seen that the method is already highly optimized and outperforms ordinary interpolation methods for many elements to be processed; however, the standalone interpolation methods with quadrature are not optimized at this point. There is a systematic difference between the source terms; the $D\Phi_p/Dt$ shows less error for the quadrature-based interpolation methods.

This analysis (see Fig. 8) investigates the effect of quadrature order of the interpolation-based

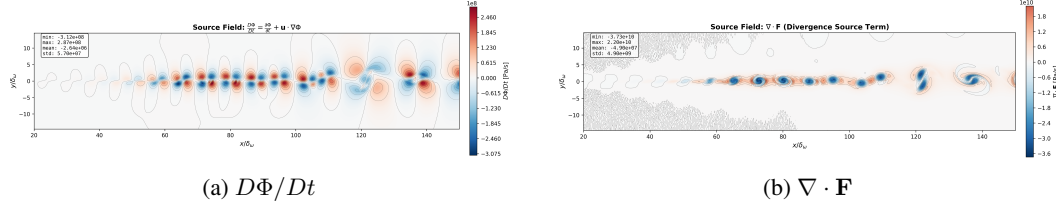


Figure 4: Source fields used for integration.

method on the accuracy of source term integration using interpolation-based B-Spline methods. The mesh resolution is fixed at $\Delta x/\delta_\omega = \Delta y/\delta_\omega = 1$. Both cubic and quintic interpolation converge

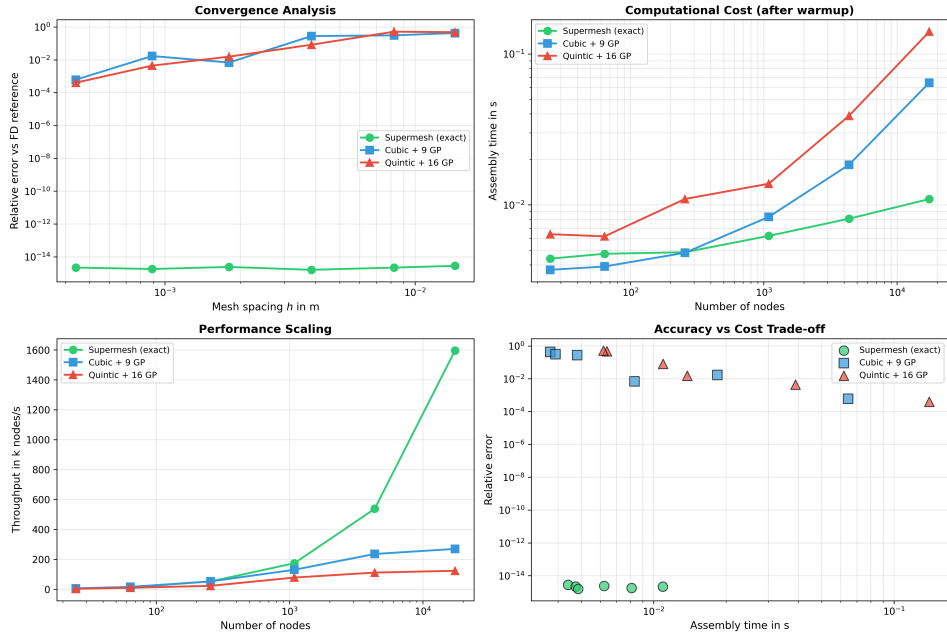


Figure 5: H-refinement analysis with CFD data for the material derivative $D\Phi_p/Dt$. Comparison between supermesh integration, cubic interpolation, and quintic interpolation.

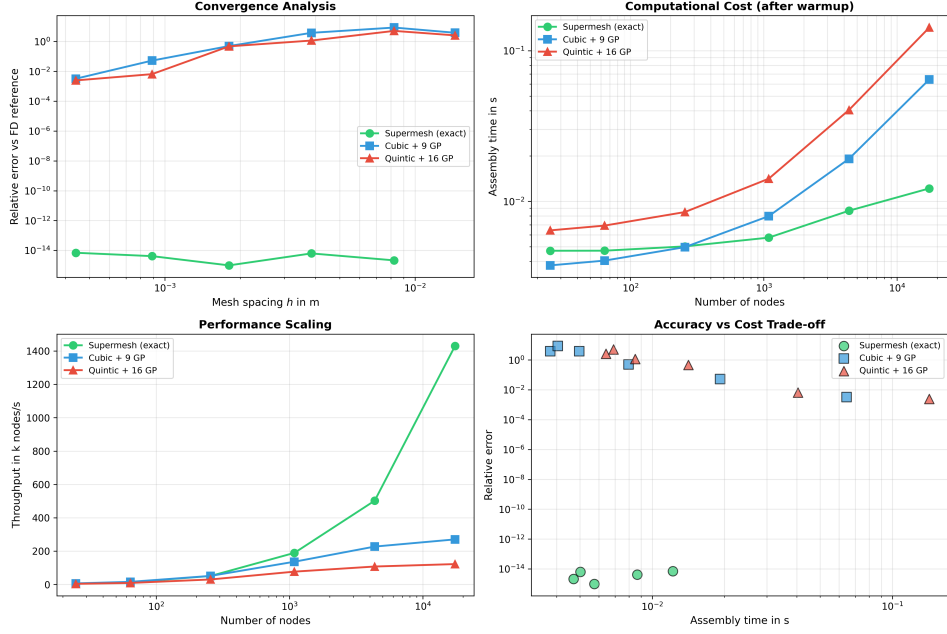


Figure 6: H-refinement analysis with CFD data for the source divergence $\nabla \cdot \mathbf{F}$. Comparison between supermesh integration, cubic interpolation, and quintic interpolation.

with increasing quadrature order but do not reach machine precision. The interpolation error for higher-order quadrature rules is dominated by the B-spline reconstruction of the finite difference field, not the quadrature error. In Figure 7, the weak scaling of the source term integration is shown, with no notable difference between the source terms.

4 Conclusions

Table 1: Comparison of integration methods for source term transformation from a finite difference grid to a finite element mesh.

	Supermesh	B-Spline
Conservation Error	Machine precision	Interpolation/Quadrature limited
Target h -Refinement	Exact at all scales	Systematic error floor (interpolation)
Primary error source	None (Geometric)	Reconstruction order of the interpolation
Mapping required	Inverse (X^{-1})	Forward (X)
Scaling	Linear (Weak)	Linear (Weak)
Source term robustness	Provided	Smoothen Sources Preferred

Acknowledgments

The authors acknowledge the support of rAI. Parts of the methods are implemented in openCFS [13], openCFS-data[14], and will be available in pyCFS-data [15] soon.

References

- [1] S. Schoder and M. Kaltenbacher. Hybrid aeroacoustic computations: State of art and new achievements. *Journal of Theoretical and Computational Acoustics*, 27(04):1950020, 2019.
- [2] S. Schoder, A. Wurzinger, C. Junger, M. Weitz, C. Freidhager, K. Roppert, and M. Kaltenbacher. Application limits of conservative source interpolation methods using a low Mach number hybrid aeroacoustic workflow. *Journal of Theoretical and Computational Acoustics*, 29(1):2050032, 2021.
- [3] M. J. Lighthill. On sound generated aerodynamically I. General theory. *Proceedings of the Royal Society of London*, 211:564–587, 1952.
- [4] Stefan Schoder, Étienne Spieser, Hugo Vincent, Christophe Boge, and Christophe Bailly. Acoustic Modeling Using the Aeroacoustic Wave Equation Based on Pierce’s Operator. *AIAA Journal*, 61(9):4008–4017, September 2023.
- [5] Stefan Schoder, Eman Bagheri, and Étienne Spieser. Aeroacoustic Source Potential Based on Poisson’s Equation. *AIAA Journal*, 62(7):2772–2782, July 2024.
- [6] S. Schoder, E. Bagheri, C. Boge, and C. Bailly. Perturbed convective wave equation for low-to-medium Mach number subsonic flows. *Journal of Sound and Vibration*, 623:119549, February 2026.
- [7] O. M. Phillips. On the generation of sound by supersonic turbulent shear layers. *Journal of Fluid Mechanics*, 9:1–18, 1960.
- [8] G. M. Lilley. On the noise from jets. Technical report, AGARD CP-131, 1974.
- [9] Maryam Babaei, Peter Rucz, Manfred Kaltenbacher, and Stefan Schoder. Super-Resolution of Elliptic PDE Solutions Using Least Squares Support Vector Regression, December 2025. arXiv:2512.09967 [math].
- [10] Ivan E. Sutherland and Gary W. Hodgman. Reentrant polygon clipping. *Communications of the ACM*, 17(1):32–42, January 1974.
- [11] Hugo Vincent and Christophe Boge. Application of the complex differentiation method to the sensitivity analysis of aerodynamic noise. *Computers & Fluids*, 264:105965, October 2023.

[12] Stefan Schoder, Manfred Kaltenbacher, Étienne Spieser, Hugo Vincent, Christophe Bogey, and Christophe Bailly. Aeroacoustic wave equation based on Pierce's operator applied to the sound generated by a mixing layer. In *28th AIAA/CEAS Aeroacoustics 2022 Conference*, Southampton, UK, June 2022. American Institute of Aeronautics and Astronautics.

[13] S. Schoder and K. Roppert. openCFS: Open source finite element software for coupled field simulation – part acoustics, 2022. *tex.archiveprefix: arxiv tex.copyright: Creative Commons Attribution 4.0 International*.

[14] Stefan Schoder and Klaus Roppert. openCFS-Data: Data Pre-Post-Processing Tool for openCFS, 2023. Version Number: 3.

[15] Andreas Wurzinger and Stefan Schoder. pyCFS-data: Data processing framework in python for openCFS. *arXiv preprint arXiv:2405.03437*, 2024.

A Reference integration by the trapezoidal rule

The 2D trapezoidal rule provides reference integration on structured finite difference grids

$$I_{\text{trap}} = \int_{\Omega} f(x, y) dx dy \approx \sum_{i=0}^{n_x-1} \sum_{j=0}^{n_y-1} w_{ij} f_{ij} \quad (22)$$

where weights w_{ij} account for grid point weighting and non-uniform spacing. For smooth functions $f \in C^2(\Omega)$, the trapezoidal rule accuracy is

$$\varepsilon_{\text{trap}} = I_{\text{exact}} - I_{\text{trap}} = \mathcal{O}(h^2) \quad (23)$$

where $h = \max(\Delta x_{\max}, \Delta y_{\max})$ is the maximum grid spacing. The weights are computed as follows for a structured grid. For grid coordinates $\{x_i\}_{i=0}^{n_x-1}$ and $\{y_j\}_{j=0}^{n_y-1}$ with spacings $\Delta x_i = x_{i+1} - x_i$ and $\Delta y_j = y_{j+1} - y_j$:

$$w_{ij} = \begin{cases} \frac{1}{4} \Delta x_0 \Delta y_0 & \text{corner: } (0, 0) \\ \frac{1}{4} \Delta x_{n_x-2} \Delta y_0 & \text{corner: } (n_x - 1, 0) \\ \frac{1}{4} \Delta x_0 \Delta y_{n_y-2} & \text{corner: } (0, n_y - 1) \\ \frac{1}{4} \Delta x_{n_x-2} \Delta y_{n_y-2} & \text{corner: } (n_x - 1, n_y - 1) \\ \frac{1}{2} \Delta x_0 \cdot \frac{1}{2} (\Delta y_{j-1} + \Delta y_j) & \text{left edge: } i = 0, j \in [1, n_y - 2] \\ \frac{1}{2} \Delta x_{n_x-2} \cdot \frac{1}{2} (\Delta y_{j-1} + \Delta y_j) & \text{right edge: } i = n_x - 1, j \in [1, n_y - 2] \\ \frac{1}{2} (\Delta x_{i-1} + \Delta x_i) \cdot \frac{1}{2} \Delta y_0 & \text{bottom edge: } i \in [1, n_x - 2], j = 0 \\ \frac{1}{2} (\Delta x_{i-1} + \Delta x_i) \cdot \frac{1}{2} \Delta y_{n_y-2} & \text{top edge: } i \in [1, n_x - 2], j = n_y - 1 \\ \frac{1}{2} (\Delta x_{i-1} + \Delta x_i) \cdot \frac{1}{2} (\Delta y_{j-1} + \Delta y_j) & \text{interior: } i, j \in [1, n - 2] \end{cases} \quad (24)$$

Algorithm Workflow

Algorithm 3 2D Trapezoidal Integration

Require: $x_{\text{fd}} \in \mathbb{R}^{n_x}$, $y_{\text{fd}} \in \mathbb{R}^{n_y}$, $f_{\text{fd}} \in \mathbb{R}^{n_y \times n_x}$
Ensure: $I_{\text{trap}} \in \mathbb{R}$

- 1: Compute spacings: $\Delta x_i = x_{i+1} - x_i$, $\Delta y_j = y_{j+1} - y_j$
- 2: Initialize weight matrix: $W \in \mathbb{R}^{n_y \times n_x}$
- 3: **for** $j = 1$ to $n_y - 2$ **do**
- 4: **for** $i = 1$ to $n_x - 2$ **do**
- 5: $W[j, i] = \frac{1}{2} (\Delta x_{i-1} + \Delta x_i) \cdot \frac{1}{2} (\Delta y_{j-1} + \Delta y_j)$
- 6: **end for**
- 7: **end for**
- 8: Compute edge weights
- 9: Compute corner weights **return** $I_{\text{trap}} = \sum_{i,j} W[j, i] \cdot f_{\text{fd}}[j, i]$

B Target element vectorized Newton-Raphson

Using isoparametric bilinear quadrilateral finite elements in 2d, the residual of the inverse mapping function is given by

$$\mathbf{R}(\boldsymbol{\xi}) = \mathbf{X}(\boldsymbol{\xi}) - \mathbf{x}^* = \sum_{j=1}^4 N_j(\boldsymbol{\xi}) \mathbf{x}_j - \mathbf{x}^* = \mathbf{0} \quad (25)$$

where, the solution $\boldsymbol{\xi}^*$ (when the residual converges to e.g. $\|\mathbf{R}\| < 10^{-10}$) can be obtained Newton-Raphson iteration

$$\boldsymbol{\xi}^{(k+1)} = \boldsymbol{\xi}^{(k)} - \mathbf{J}^{-1}(\boldsymbol{\xi}^{(k)}) \mathbf{R}(\boldsymbol{\xi}^{(k)}), \quad (26)$$

where the gradient of the residual is defined by the Jacobian $\mathbf{J}(\boldsymbol{\xi}) = \frac{\partial \mathbf{R}}{\partial \boldsymbol{\xi}} = \frac{\partial \mathbf{X}}{\partial \boldsymbol{\xi}}$.

This can be efficiently implemented using a vectorized Newton-Raphson scheme that processes all quadrature points for an element j -index summation. Use the physical coordinates $\mathbf{x}_{in} = [x_1, \dots, x_n]^T$, $\mathbf{y}_{in} = [y_1, \dots, y_n]^T$ with a batch number of n points.

$$\mathbf{F}_x^{(k)} = \sum_{j=1}^4 N_j(\boldsymbol{\xi}_r^{(k)}, \boldsymbol{\eta}_r^{(k)}) x_j - \mathbf{x}_{in} \quad (27)$$

$$\mathbf{F}_y^{(k)} = \sum_{j=1}^4 N_j(\boldsymbol{\xi}_r^{(k)}, \boldsymbol{\eta}_r^{(k)}) y_j - \mathbf{y}_{in} \quad (28)$$

$$\mathbf{J}_{11}^{(k)} = \sum_{j=1}^4 \frac{\partial N_j}{\partial \xi_r}(\boldsymbol{\xi}_r^{(k)}, \boldsymbol{\eta}_r^{(k)}) x_j \quad (29)$$

$$\mathbf{J}_{12}^{(k)} = \sum_{j=1}^4 \frac{\partial N_j}{\partial \eta_r}(\boldsymbol{\xi}_r^{(k)}, \boldsymbol{\eta}_r^{(k)}) x_j \quad (30)$$

$$\mathbf{J}_{21}^{(k)} = \sum_{j=1}^4 \frac{\partial N_j}{\partial \xi_r}(\boldsymbol{\xi}_r^{(k)}, \boldsymbol{\eta}_r^{(k)}) y_j \quad (31)$$

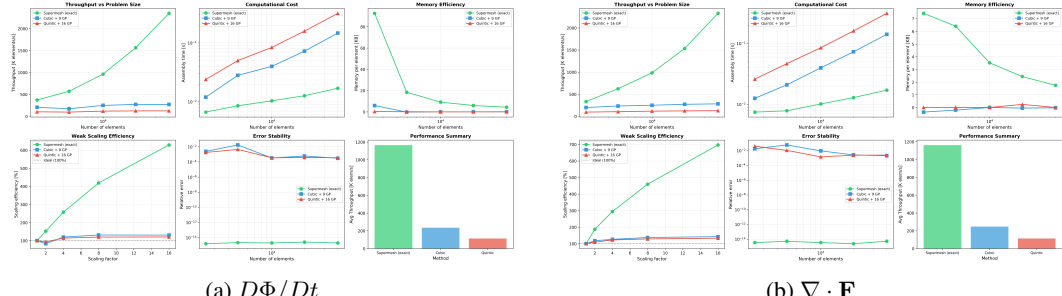
$$\mathbf{J}_{22}^{(k)} = \sum_{j=1}^4 \frac{\partial N_j}{\partial \eta_r}(\boldsymbol{\xi}_r^{(k)}, \boldsymbol{\eta}_r^{(k)}) y_j \quad (32)$$

$$\det(\mathbf{J})^{(k)} = \mathbf{J}_{11}^{(k)} \mathbf{J}_{22}^{(k)} - \mathbf{J}_{12}^{(k)} \mathbf{J}_{21}^{(k)} \quad (33)$$

$$\boldsymbol{\xi}_r^{(k+1)} = \boldsymbol{\xi}_r^{(k)} - \frac{\mathbf{J}_{22}^{(k)} \mathbf{F}_x^{(k)} - \mathbf{J}_{12}^{(k)} \mathbf{F}_y^{(k)}}{\det(\mathbf{J})^{(k)}} \quad (34)$$

$$\boldsymbol{\eta}_r^{(k+1)} = \boldsymbol{\eta}_r^{(k)} - \frac{\mathbf{J}_{11}^{(k)} \mathbf{F}_y^{(k)} - \mathbf{J}_{21}^{(k)} \mathbf{F}_x^{(k)}}{\det(\mathbf{J})^{(k)}} \quad (35)$$

C Weak Scaling



(a) $D\Phi/Dt$

(b) $\nabla \cdot \mathbf{F}$

Figure 7: Weak scaling analysis with CFD data.

D Interpolation Study

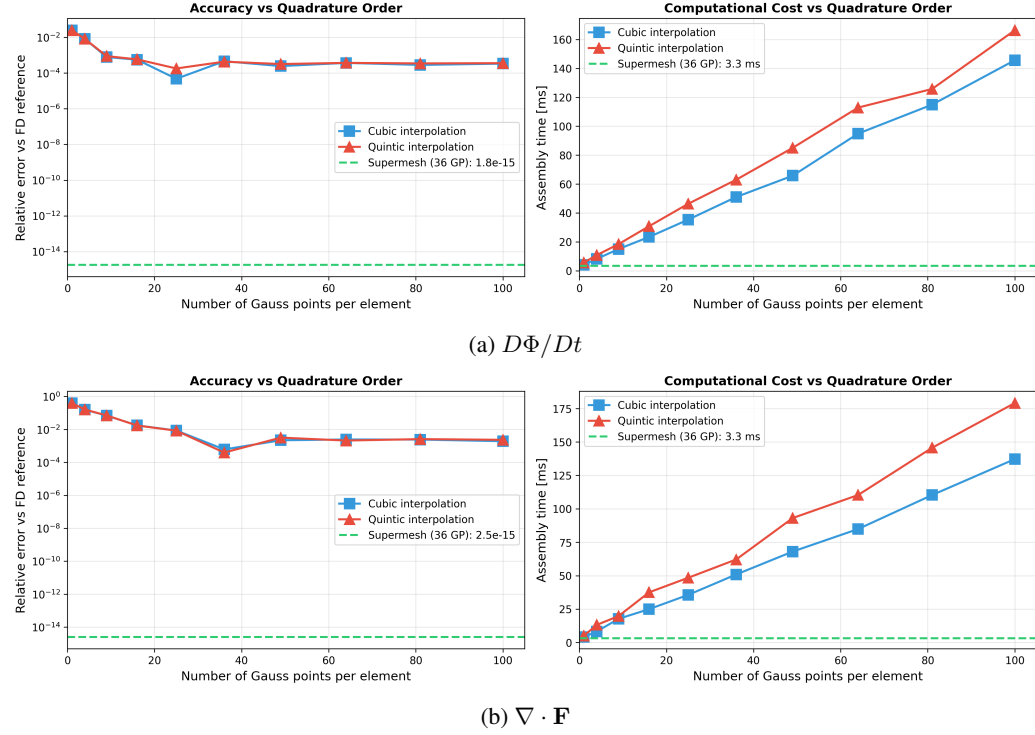


Figure 8: Effect of quadrature order on integration accuracy. The horizontal dashed line indicates the supermesh reference accuracy.